



# Crystallographic and Optical Characteristics of Ultraviolet-Stimulated Dy<sup>3+</sup>-Doped Ba<sub>2</sub>GdV<sub>3</sub>O<sub>11</sub> Nanorods

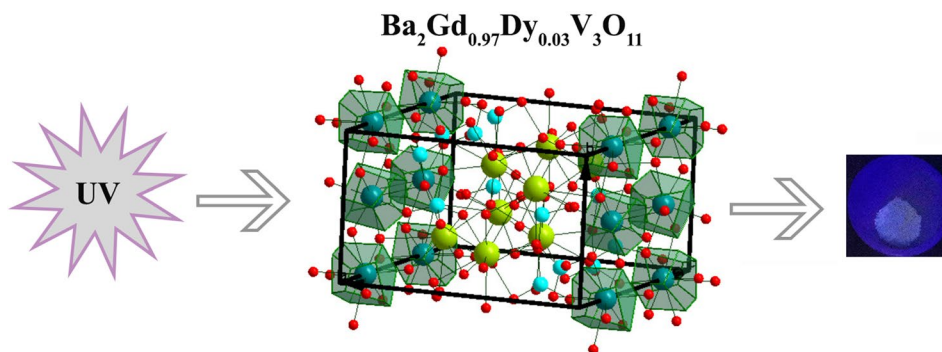
Priya Phogat<sup>1</sup> · V. B. Taxak<sup>1</sup> · R. K. Malik<sup>1</sup>

Received: 10 August 2021 / Accepted: 9 May 2022 / Published online: 31 May 2022  
© The Minerals, Metals & Materials Society 2022

## Abstract

A ultraviolet-triggered white light-emitting Ba<sub>2</sub>Gd<sub>1-x</sub>V<sub>3</sub>O<sub>11</sub>:xDy<sup>3+</sup> nanophosphor series has been developed with the aid of urea-fueled solution combustion route, for the first time. Powder x-ray diffraction and Rietveld refinement have been utilized to study the structural features of the synthesized series. Transmission electron microscopy (TEM), field emission scanning electron microscopy (FE-SEM), and energy-dispersive spectroscopy (EDS) analysis have been employed for morphological and elemental analysis. When triggered by ultraviolet radiation at 324 nm, the Dy<sup>3+</sup>-doped nanophosphor exhibited characteristic peaks attributed to emissions due to <sup>4</sup>F<sub>9/2</sub> → <sup>6</sup>H<sub>13/2, 15/2</sub> transitions. The concentration quenching phenomenon was witnessed for the 3 mol% fluorescent composition in Dy<sup>3+</sup>-doped Ba<sub>2</sub>GdV<sub>3</sub>O<sub>11</sub> nanophosphor. The Auzel's model has been of great usage in determining the values for intrinsic lifetime (1.112 ms) and non-radiative rates (421.178 s<sup>-1</sup>). The efficient and cool conduct of the white light-emitting nanophosphor series has been endorsed by the CIE color coordinates (x = 0.256, y = 0.341), correlated color temperature (CCT = 9751 K), and quantum efficiency value (67%). The structural and photoluminescence behavior featured by the trivalent dysprosium-doped Ba<sub>2</sub>GdV<sub>3</sub>O<sub>11</sub> nanophosphor support its usage in ultraviolet-stimulated lighting devices.

## Graphical Abstract



**Keywords** Ba<sub>2</sub>GdV<sub>3</sub>O<sub>11</sub>:Dy<sup>3+</sup> · WLEDs · non-radiative rate · nanophosphor · photoluminescence

## Introduction

The origin and evolution of life forms on Earth has been heavily dependent upon the Sun, a natural source of light that is well known for shaping the habits of living organisms on the planet. Early humans made a significant and remarkable discovery of fire. This major breakthrough led to the manifestation of light in a form other than that of

✉ R. K. Malik  
lion.singh0108@gmail.com

<sup>1</sup> Department of Chemistry, Maharshi Dayanand University,  
Rohtak 124001, India

natural sources. Human civilizations are known to ignite fires using different fuels and exploit this artificial source of lighting to the fullest. In recent history, artificial light sources such as gas lamps, electric lamps, incandescent light bulbs, and high-intensity discharge (HID) lamps have been invented. Among these the HID lamps, compact fluorescent lamps (CFLs), high-pressure sodium lamps, and metal-halide lamps are the most advanced and successful types.<sup>1–3</sup> The latter half of the twentieth century witnessed the invention of a solid-state lighting (SSL) technology, far more advanced than its counterparts. This invention, namely, the light-emitting diode (LED), produces light from electricity using a semiconductor material. White light-emitting diodes (WLEDs) are known today for their sturdiness and high-quality light production. The global demand for energy conservation looks at WLEDs as an energy savior. Qualities such as less power usage, long life span, and energy efficiency have made WLEDs quite popular among households, industries, and research units. WLEDs are of great advantage for lighting, displays, and biomedical applications.<sup>4–6</sup>

The fabrication process of a WLED plays a crucial role in its resulting properties. On an established note, a yellow light-emitting cerium-doped yttrium aluminum garnet ( $\text{Ce}^{3+}:\text{YAG}$ ) is coated upon a blue light-emitting indium gallium nitride (InGaN) chip. The emitted blue light excites the yellow phosphor and produces white light.<sup>7,8</sup> However, fabrication through this conventional route involves some disadvantages, namely, insufficient red constituent in the emission spectra and low color rendering index (CRI) ( $R_a < 80$ ).<sup>9,10</sup> Another route of fabrication has been followed in order to deal with the abovementioned inadequacies. The ultraviolet/near-ultraviolet (UV/NUV)-emitting chip is used in place of the blue-emitting InGaN chip along with a collection of phosphors with individual red, green, and blue emission. As the three different phosphors display different decay times, an intense white emission is not observed.<sup>11,12</sup> Thus, a single white light-emitting phosphor, excitable by UV or NUV radiation, is a good choice to fabricate WLEDs. Consequently, good luminescence, chemical stability, and efficient UV/NUV absorption are some of the qualities that a white light-emitting phosphor should exhibit.<sup>13,14</sup> Such phosphor materials need to be explored, studied, and potentially used in the fabrication of WLEDs.

An efficient white light-emitting material can be synthesized by packing a stable host and an appropriate luminescent ion together. The metals known as rare earths are well known to absorb UV/NUV radiation in an effective manner. Different color emissions can be obtained by switching the rare earth metals or ions as dopants.<sup>15–17</sup> The nature of the host lattice is crucial to the stability and integrity of the synthesized nanophosphor. Hence, a number of borate-, nitride-,

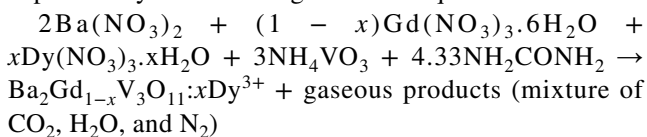
sulfide-, and vanadate-based host materials are studied and thoroughly analyzed.<sup>18,19</sup> Among the abovementioned materials, the ones comprising a vanadate group are known to form a stable lattice at lower synthesizing temperatures and aid effectively in the luminescence exhibited by the nanophosphor by transfer of energy from vanadate to the dopant unit.<sup>20</sup> These qualities suffice for the vanadate-based host to be considered as an effective host material for the synthesis of nanophosphor. The trivalent rare earth ion  $\text{Dy}^{3+}$  is well known for its absorption of radiation falling in the ultraviolet region and emitting bright white light due to its characteristic  ${}^4\text{F}_{9/2} \rightarrow {}^6\text{H}_{13/2, 15/2}$  transitions.<sup>21</sup> The above discussion points in favor of doping a vanadate-based host with trivalent dysprosium ions in order to achieve a stable, crystalline, and efficient white light-emitting nanophosphor. According to the literature survey, there are two reports on rare earth-doped  $\text{Ba}_2\text{GdV}_3\text{O}_{11}$ ,<sup>22,23</sup> but there has not been a single work reported on  $\text{Dy}^{3+}$ -doped  $\text{Ba}_2\text{GdV}_3\text{O}_{11}$  nanophosphor. The present report is focused on preparing a homogenous  $\text{Dy}^{3+}$ -doped  $\text{Ba}_2\text{GdV}_3\text{O}_{11}$  nanophosphor series at  $900^\circ\text{C}$  by means of a time-saving (calcination time = 3 h) solution combustion route. In the literature, the rare earth-doped compositions of  $\text{Ba}_2\text{GdV}_3\text{O}_{11}$  nanophosphor were synthesized by sol–gel approach constituting 48 h of reaction for gel formation and 3-h-long calcination of the sample in a temperature range of  $600^\circ\text{C}$ – $800^\circ\text{C}$ .<sup>22</sup> In the current report, detailed structural, optical, and decay behavior analyses have been performed exclusively. A thorough photometric and decay analysis for trivalent dysprosium-doped  $\text{Ba}_2\text{GdV}_3\text{O}_{11}$  nanophosphor has also been carried out in present report, as original work.

An energy-efficient method of solution combustion has been utilized to prepare the nanophosphor series of  $\text{Ba}_2\text{Gd}_{1-x}\text{V}_3\text{O}_{11}:x\text{Dy}^{3+}$  ( $x = 0.01$ – $0.09$ ). The Rietveld refinement explored the aspects of coordination of various entities as well as crystal system of the synthesized nanophosphor. The energy transfer phenomenon has been explored via calculations of parameters such as critical distance ( $R_c$ ) of energy transfer. Different techniques such as transmission electron microscopy (TEM), field emission scanning electron microscopy (FE-SEM), and energy-dispersive spectroscopy (EDS) have been employed for morphological plus elemental analysis. The photoluminescence and decay behavior exhibited by the  $\text{Ba}_2\text{Gd}_{1-x}\text{V}_3\text{O}_{11}:x\text{Dy}^{3+}$  nanophosphor have been investigated via excitation emission and decay curves, respectively. The values for radiative rates, quantum efficiency, and non-radiative rates have been attained for a complete series of  $\text{Ba}_2\text{Gd}_{1-x}\text{V}_3\text{O}_{11}:x\text{Dy}^{3+}$  ( $x = 0.01$ – $0.09$ ) nanophosphor. The CIE  $x$ ,  $y$  coordinates as well as CCT (K) values confirm the  $\text{Dy}^{3+}$ -doped  $\text{Ba}_2\text{GdV}_3\text{O}_{11}$  nanophosphor as a useful candidate for UV-triggered lighting sources.

## Experimental

### Materials and Synthesis

Solution combustion synthesis was employed to prepare the entire nanophosphor series of Dy<sup>3+</sup>-doped Ba<sub>2</sub>GdV<sub>3</sub>O<sub>11</sub> nanophosphor. The time-saving and energy-efficient route led to highly crystalline and homogeneous nanophosphor product.<sup>24–26</sup> The initial step implied the procurement of highly pure chemicals, namely, Dy(NO<sub>3</sub>)<sub>3</sub>·xH<sub>2</sub>O, Ba(NO<sub>3</sub>)<sub>2</sub>, Gd(NO<sub>3</sub>)<sub>3</sub>·6H<sub>2</sub>O, NH<sub>4</sub>VO<sub>3</sub>, and urea. The ammonium vanadate and different metal nitrates acting as oxidizers were weighed in accordance to the ratio of oxidizer and fuel taken as one. The reactants after proper weighing were dissolved in an appropriate amount of deionized water reserved in a Pyrex beaker (250 mL). The beaker was then placed on a hot plate (150°C) for a time span of 5 min. The heat aided in dissolving the reactants properly. The Pyrex beaker containing the homogeneous solution was subjected to a temperature of 500°C for h inside a muffle furnace. After 0.5 h, the Pyrex beaker was removed from the muffle furnace, and the contents were cooled to room temperature. It was observed that the homogeneous solution had turned into a voluminous powder. The powder, following a fine crushing, was transferred to an alumina crucible and put into a furnace set at 900°C. Later, after 3 h, the alumina crucible was subjected to room temperature, and its content was allowed to cool down. The content was finely ground to a powder form and saved in a desiccator for characterization procedures. Different compositions of the Ba<sub>2</sub>Gd<sub>1-x</sub>Dy<sub>x</sub>V<sub>3</sub>O<sub>11</sub> nanophosphor series were prepared via the aforementioned route, as explained by the following chemical equation:



### Methods of Characterization

The entire Ba<sub>2</sub>Gd<sub>1-x</sub>V<sub>3</sub>O<sub>11</sub>:x Dy<sup>3+</sup> (x = 0.01–0.09) nanophosphor series was synthesized via an efficient route of solution combustion. The patterns due to diffraction exhibited by the individual compositions were used to analyze the phase purity of the prepared nanophosphors. A Rigaku Ultima-IV labeled powder diffractometer working at high resolution with x-rays irradiated from Cu K $\alpha$  with a 40-mA tube current and voltage of 40 kV was employed to document x-ray diffraction (XRD) patterns in a continuous scanning fashion at rate of 2° per minute from an angular range of 10° to 80°. The XRD data of the

optimal fluorescent composition was analyzed via Rietveld refinement. In order to do so, a pseudo-Voigt function was applied in the software program General Structure Analysis System (GSAS).

An FEI Tecnai TF20 labeled transmission electron microscope recorded the TEM and high-resolution transmission electron microscopy (HRTEM) micrographs of Ba<sub>2</sub>Gd<sub>1-x</sub>V<sub>3</sub>O<sub>11</sub>:xDy<sup>3+</sup> nanophosphor. The surface of the synthesized sample was analyzed via field emission scanning electron microscopy (FE-SEM) using an FEI Quanta 200 consisting of an intense field-emission gun (FEG) as the source and an Everhart–Thornley detector. The sample surface was scanned with a high-energy electron beam in a raster scan pattern. The elemental analysis was performed using the Oxford EDS system IE 250 X Max 80 with a silicon drift detector (SDD). A fluorescence spectrophotometer marked as Hitachi F-7000 was used to study the photoluminescence spectra of the Dy<sup>3+</sup>-doped Ba<sub>2</sub>GdV<sub>3</sub>O<sub>11</sub> nanophosphor. A wavelength scan at a rate of 1200 nm/min was run at a 400-V photomultiplier tube (PMT) voltage, and 5 nm was the slit width to record the excitation and emission spectra of the Ba<sub>2</sub>Gd<sub>1-x</sub>V<sub>3</sub>O<sub>11</sub>:xDy<sup>3+</sup> (x = 0.01–0.09) nanophosphor series. The decay curves were recorded by a time scan at a chopping speed of 40 Hz and a response time of 2 ms with abovementioned conditions of voltage and slit width. The color coordinates (x, y) of the optimal luminescent composition of Ba<sub>2</sub>Gd<sub>0.97</sub>Dy<sub>0.03</sub>V<sub>3</sub>O<sub>11</sub> were conveyed via the CIE 1931 chromaticity diagram. The u', v' coordinates and CCT values were also calculated.

## Results and Discussion

### Structural Studies

An energy-efficient method of solution combustion was followed to formulate a homogenous and crystalline Ba<sub>2</sub>Gd<sub>1-x</sub>V<sub>3</sub>O<sub>11</sub>:xDy<sup>3+</sup> (x = 0.01–0.09) nanophosphor series. The XRD patterns for both pure host and doped composition were obtained by x-ray investigation and detected to be in close accord to that of standard JCPDS card no. 45-0097 for Ba<sub>2</sub>GdV<sub>3</sub>O<sub>11</sub> pure host, as depicted in Fig. 1. The trivalent dysprosium ion is supposed to replace the trivalent gadolinium ion on doping owing to similar charges and ionic radii. This assumption can be reasoned by calculating the radius percentage difference ( $\Delta_r$ ) by the following equation:

$$\Delta_r = \frac{R_m(\text{CN}) - R_d(\text{CN})}{R_m(\text{CN})} \times 100 \quad (1)$$

In Eq. 1,  $\Delta_r$  stands for the percentage difference in radius,  $R_m(\text{CN})$  signifies the effective ionic radii corresponding to

host ions,  $R_d(CN)$  represents the effective ionic radii analogous to dopant ions. Also,  $CN$  symbolizes the coordination number of the concerned ion. The coordination exhibited by both  $Dy^{3+}$  and  $Gd^{3+}$  ions in  $Ba_2Gd_{1-x}Dy_xV_3O_{11}$  nanophosphor is seven ( $CN = 6$ ). In the present case, the magnitude for radius percentage difference ( $\Delta_r$ ) comes out to be 2.77%. Also, the approved value of  $\Delta_r$  is less than 30%.<sup>27</sup> Therefore,  $Dy^{3+}$  dopant ions replace  $Gd^{3+}$  in the host lattice. The assumptions of  $Ba^{2+}$  or  $V^{5+}$  ions being replaced by dopant ions cannot be approved due to dissimilarity in

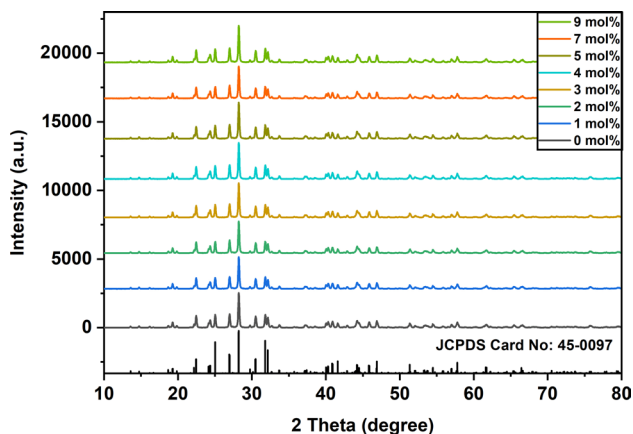


**Fig. 1** XRD pattern of  $Ba_2Gd_{1-x}Dy_xV_3O_{11}$  ( $x = 0 - 0.09$ ) nanophosphor system along with the standard data of  $Ba_2GdV_3O_{11}$  host lattice.

their charge, size, coordination, and large value of radius percentage difference.

Rietveld refinement was performed on XRD data of  $0.03Dy^{3+}:Ba_2Gd_{0.97}V_3O_{11}$  nanophosphor (Fig. 2). The refined graph consists of a regular red line (experimental data set), an irregular square-shaped line (observed data set), and a navy-bluish line exhibiting the difference between the previously mentioned lines. The pattern was refined up to  $\chi^2 = 2.076$ . Different parameters relative to lattice, namely  $a = 12.3932(12)$  Å,  $b = 7.7317(7)$  Å,  $c = 11.1786(11)$  Å, and  $V = 1042.51(11)$  Å<sup>3</sup>, were obtained and listed in Table I. There was an observed increase in density of the doped composition due to increase in formula weight and a subsequent decrease in volume on replacing  $Gd^{3+}$  ions (larger ionic radii) with dopant  $Dy^{3+}$  ions (smaller ionic radii). The ion types and the respective occupancy are depicted in Table II. There are two types of Ba atomic sites (Ba1 and Ba2), one type of Gd/Dy site (Gd1/Dy1), and three types of V sites (V1, V2 and V3). Ba1, Ba2, and Gd/Dy bear a coordination number of ten, 11, and six, respectively (Fig. 3). There are present both  $VO_4^{3-}$  and  $V_2O_7^{4-}$  groups in  $Ba_2Gd_{1-x}Dy_xV_3O_{11}$  nanophosphor. All V sites were found to have a coordination number of four and coordinated in a tetrahedral fashion. The homogenous powder form of synthesized nanophosphor may consist of agglomerated particles, and hence, the average crystallite size of the particles of synthesized  $Dy^{3+}:Ba_2GdV_3O_{11}$  nanophosphor was estimated using the renowned Scherrer equation<sup>28</sup> as follows:

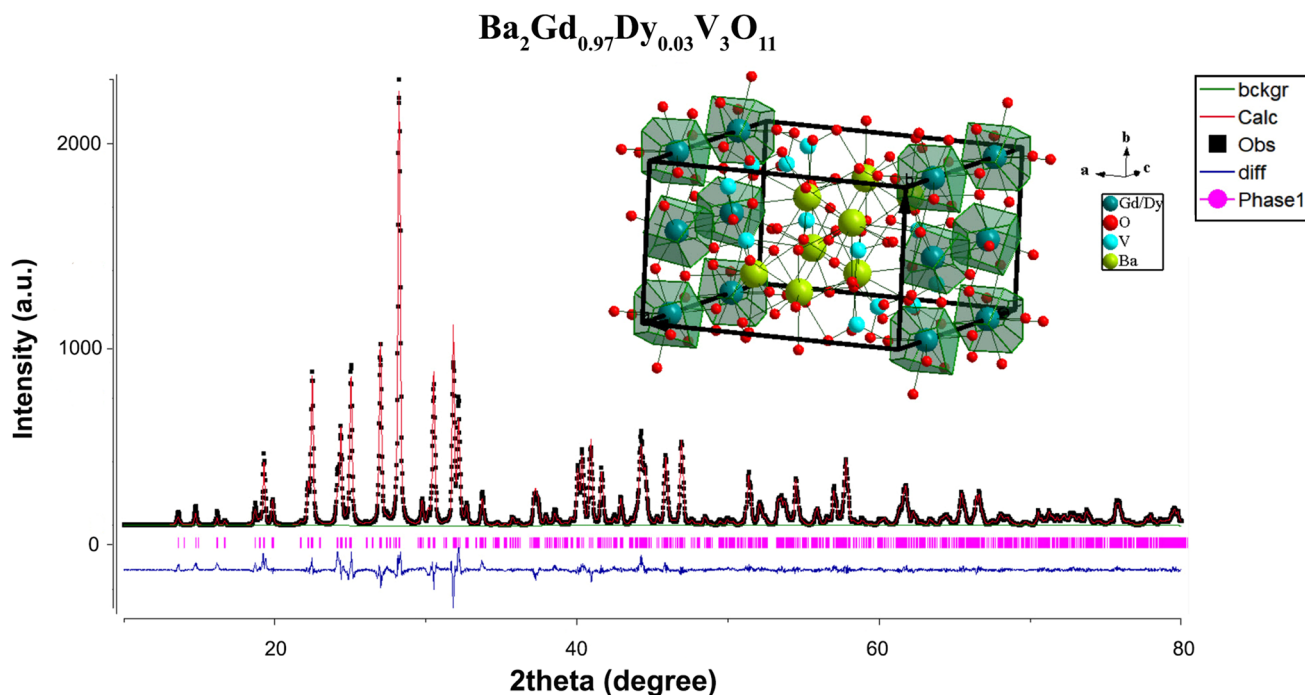


**Fig. 2** Rietveld refinement of  $Ba_2Gd_{0.93}Dy_{0.03}V_3O_{11}$  nanophosphors.  $\chi^2 = 2.076$ ,  $R_{wp}$  (%) = 11.87, and  $R_p$  (%) = 7.81.

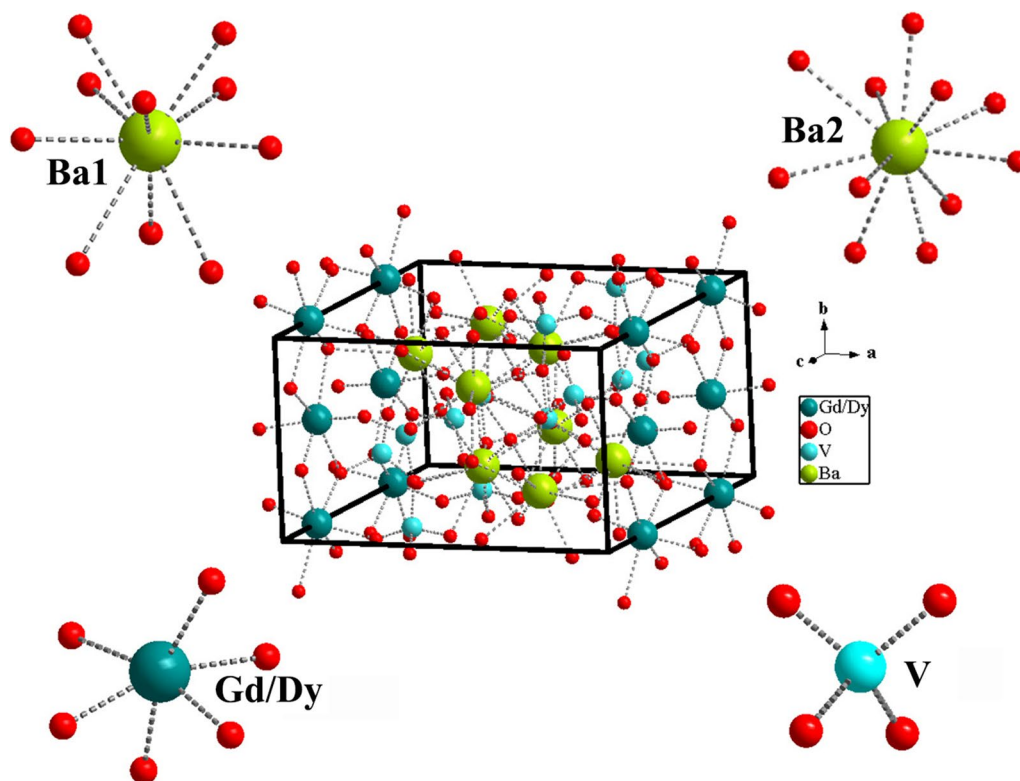


**Fig. 3** Unit cell view of Ba<sub>2</sub>Gd<sub>1-x</sub>Dy<sub>x</sub>V<sub>3</sub>O<sub>11</sub> nanocrystals along with the coordinative environment of various cations.

**Table 1** Crystal structure data and goodness of fit for Ba<sub>2</sub>Gd<sub>0.97</sub>Dy<sub>0.03</sub>V<sub>3</sub>O<sub>11</sub> phosphor system as compared to Ba<sub>2</sub>GdV<sub>3</sub>O<sub>11</sub> host matrix

Formula	Ba <sub>2</sub> Gd <sub>0.97</sub> Dy <sub>0.03</sub> V <sub>3</sub> O <sub>11</sub>	Ba <sub>2</sub> GdV <sub>3</sub> O <sub>11</sub> <sup>23</sup>
Formula weight (g mol <sup>-1</sup> )	760.88	760.72
Crystal system	Monoclinic	Monoclinic
Space group symmetry	<i>P21/c</i> (14)	<i>P21/c</i> (14)
<i>a</i> (Å)	12.3932(12)	12.3400
<i>b</i> (Å)	7.7317(7)	7.7420
<i>c</i> (Å)	11.1786(11)	11.2490
$\alpha = \gamma$ (degree)	90	90
$\beta$ (degree)	103.277	103.300
Volume (Å <sup>3</sup> )	1042.51(11)	1045.86
<i>Z</i>	4	4
Density (g cm <sup>-3</sup> )	4.84752	4.8308
Pearson code	mP68	mP68
Wyckoff sequence	e17	e17

$$D = \frac{0.941\lambda}{\beta \cos \theta} \quad (2)$$

In the abovementioned equation, *D* stands for the average crystallite size,  $\lambda$  symbolizes the x-ray wavelength set for the diffractometer (= 0.1540562 nm), and  $\beta$  represents

the full width of the diffraction line at an intensity value half of the maximum for the most intense peak, whereas  $\theta$  signifies that angle where the most intense peak is positioned. The average size of crystallite corresponding to the Ba<sub>2</sub>Gd<sub>1-x</sub>V<sub>3</sub>O<sub>11</sub>:xDy<sup>3+</sup> ( $x = 0.01$ – $0.09$ ) nanophosphor was estimated to be 34 nm.

The synthesized trivalent dysprosium-doped nanophosphor was analyzed through HRTEM, and the results are depicted in Fig. 4a and b. The HRTEM result consists of planes with interplanar distance of 0.311 nm that equates to a diffraction plane of (12 $\bar{2}$ ) Ba<sub>2</sub>Gd<sub>1-x</sub>V<sub>3</sub>O<sub>11</sub>:xDy<sup>3+</sup> nanophosphor. The TEM (Fig. 4b) and FE-SEM (Fig. 4c) results represent rod-like structures with a diameter in the nano range. The EDS) analysis result provided a graph with peaks corresponding to the elements present in the platinum-coated sample of prepared nanophosphor Ba<sub>2</sub>GdV<sub>3</sub>O<sub>11</sub>:Dy<sup>3+</sup> (Fig. 5). There was no other peak than the respective elements, and hence, the synthesized nanophosphor is free from any kind of impurity. The nanophosphor was synthesized through solution combustion route and that is known for homogenous product formation.<sup>29,30</sup> In order to analyze the uniform distribution of various chemical components, elemental mapping was performed. Figure 6 indicates a homogenous nature of the synthesized Ba<sub>2</sub>GdV<sub>3</sub>O<sub>11</sub>:Dy<sup>3+</sup> nanophosphor via elemental mapping.

**Table II** Various ion types and occupancy in  $\text{Ba}_2\text{Gd}_{0.97}\text{Dy}_{0.03}\text{V}_3\text{O}_{11}$  nanophosphor

Label	Ion type	Site	Occupancy	Label	Ion type	Site	Occupancy
Ba1	$\text{Ba}^{2+}$	4e	1	O3	$\text{O}^{2-}$	4e	1
Ba2	$\text{Ba}^{2+}$	4e	1	O4	$\text{O}^{2-}$	4e	1
V1	$\text{V}^{5+}$	4e	1	O5	$\text{O}^{2-}$	4e	1
V2	$\text{V}^{5+}$	4e	1	O6	$\text{O}^{2-}$	4e	1
V3	$\text{V}^{5+}$	4e	1	O7	$\text{O}^{2-}$	4e	1
Gd1	$\text{Gd}^{3+}$	4e	0.97	O8	$\text{O}^{2-}$	4e	1
Dy1	$\text{Dy}^{3+}$	4e	0.03	O9	$\text{O}^{2-}$	4e	1
O1	$\text{O}^{2-}$	4e	1	O10	$\text{O}^{2-}$	4e	1
O2	$\text{O}^{2-}$	4e	1	O11	$\text{O}^{2-}$	4e	1

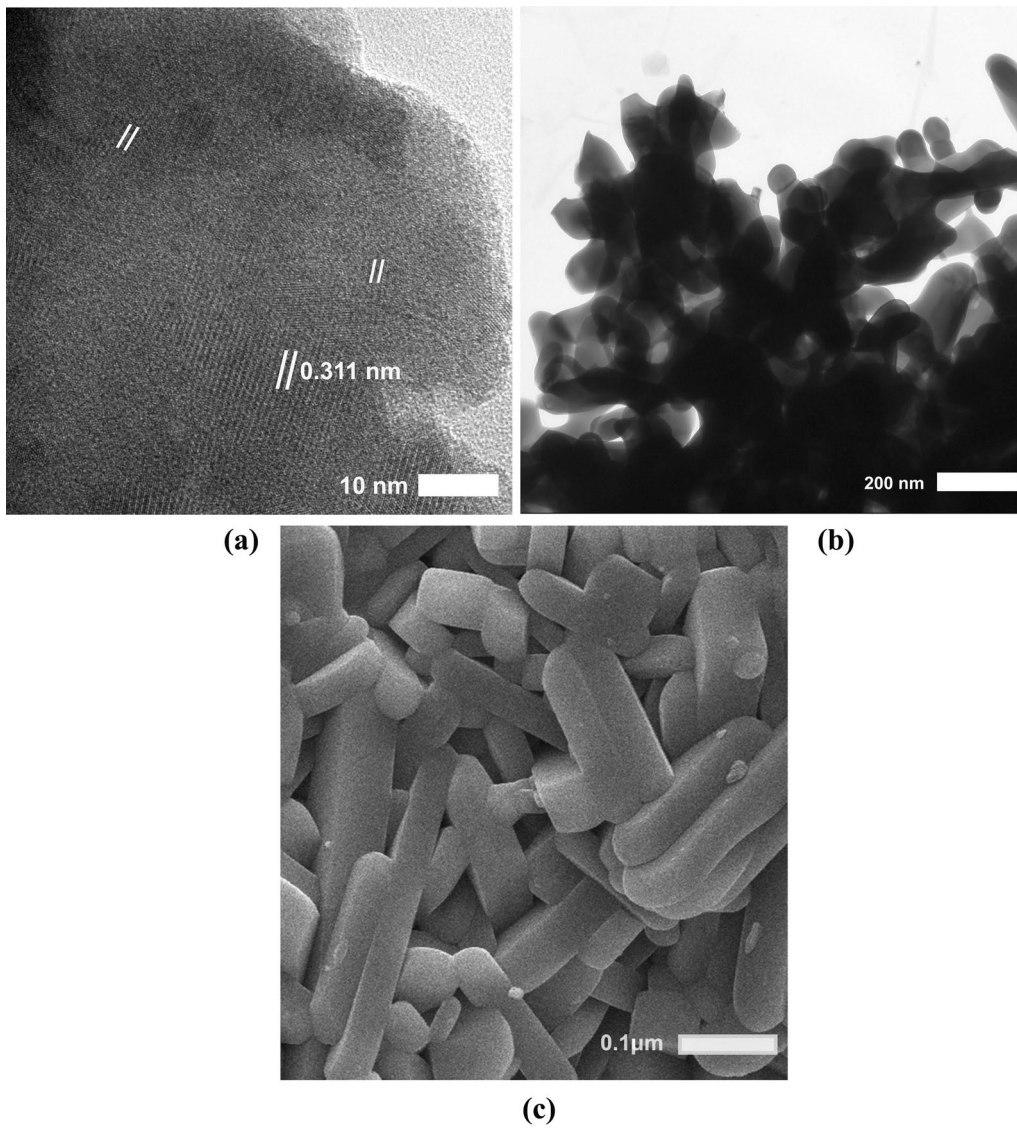


**Fig. 4** (a) HRTEM, (b) TEM, and (c) FE-SEM images of  $\text{Ba}_2\text{Gd}_{1-x}\text{Dy}_x\text{V}_3\text{O}_{11}$  nanophosphor.

## Photoluminescence Analysis

Different mol% compositions of the Ba<sub>2</sub>Gd<sub>1-x</sub>Dy<sub>x</sub>V<sub>3</sub>O<sub>11</sub> ( $x = 0.01-0.09$ ) nanophosphor series were prepared by solution combustion method, and the respective excitation/emission spectra and decay curves were documented on a fluorescence spectrophotometer using a running wavelength and time scan, respectively. The excitation spectra of Ba<sub>2</sub>Gd<sub>1-x</sub>Dy<sub>x</sub>V<sub>3</sub>O<sub>11</sub> nanophosphors at emission

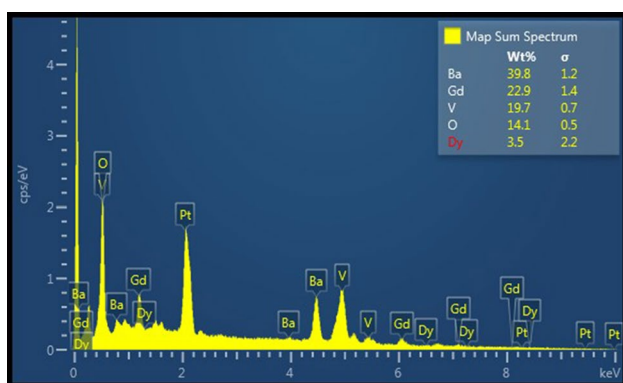


Fig. 5 EDS analysis of Ba<sub>2</sub>GdV<sub>3</sub>O<sub>11</sub>:Dy<sup>3+</sup> nanophosphor.

wavelength of 573 nm are displayed in Fig. 7. There is an intense band centered at 324 nm that is attributed to the absorption of host. As the wavelength proceeds towards 500 nm, multiple other bands arise in the excitation spectra due to characteristic  $f-f$  transitions of dopant Dy<sup>3+</sup> ions. These include four small bands centered at 351 nm, 365 nm, 389 nm, and 427 nm and two broad peaks at 453 and 474 nm. The most intense band with maxima at 324 nm arises in the excitation spectra due to  $^1A_1 \rightarrow ^1T_{1,2}$  transition in the VO<sub>4</sub><sup>3-</sup> group of host. The VO<sub>4</sub><sup>3-</sup> unit of the host comprises a ground-state term ( $^1A_1$ ), two singlet excited-state terms ( $^1T_1$ ,  $^1T_2$ ), and two triplet excited-state terms ( $^3T_1$ ,  $^3T_2$ ).<sup>31,32</sup> A broad band at 324 nm indicates that the singlet excited states ( $^1T_1$ ,  $^1T_2$ ) are closer in energy; hence, rather than two separate peaks, a broad band arises due to  $^1A_1 \rightarrow ^1T_{1,2}$  transitions. Furthermore, the small bands at 351 nm, 365 nm, 389 nm, and 427 nm are attributed to  $^6H_{15/2} \rightarrow ^6P_{7/2}$ ,  $^6P_{5/2}$ ,  $^4I_{13/2}$ , and  $^4G_{11/2}$  transitions, respectively, whereas the broad peaks centered at 453 and 474 nm arise due to  $^6H_{15/2} \rightarrow ^4I_{15/2}$  and  $^6H_{15/2} \rightarrow ^4F_{9/2}$  characteristic transition of Dy<sup>3+</sup> ions.<sup>33</sup> In the excitation spectra from 200 to 500 nm, the charge transfer band due to  $^1A_1 \rightarrow ^1T_{1,2}$  transition is the most intense. This excitation at 324 nm brands the synthesized nanophosphor as suitable

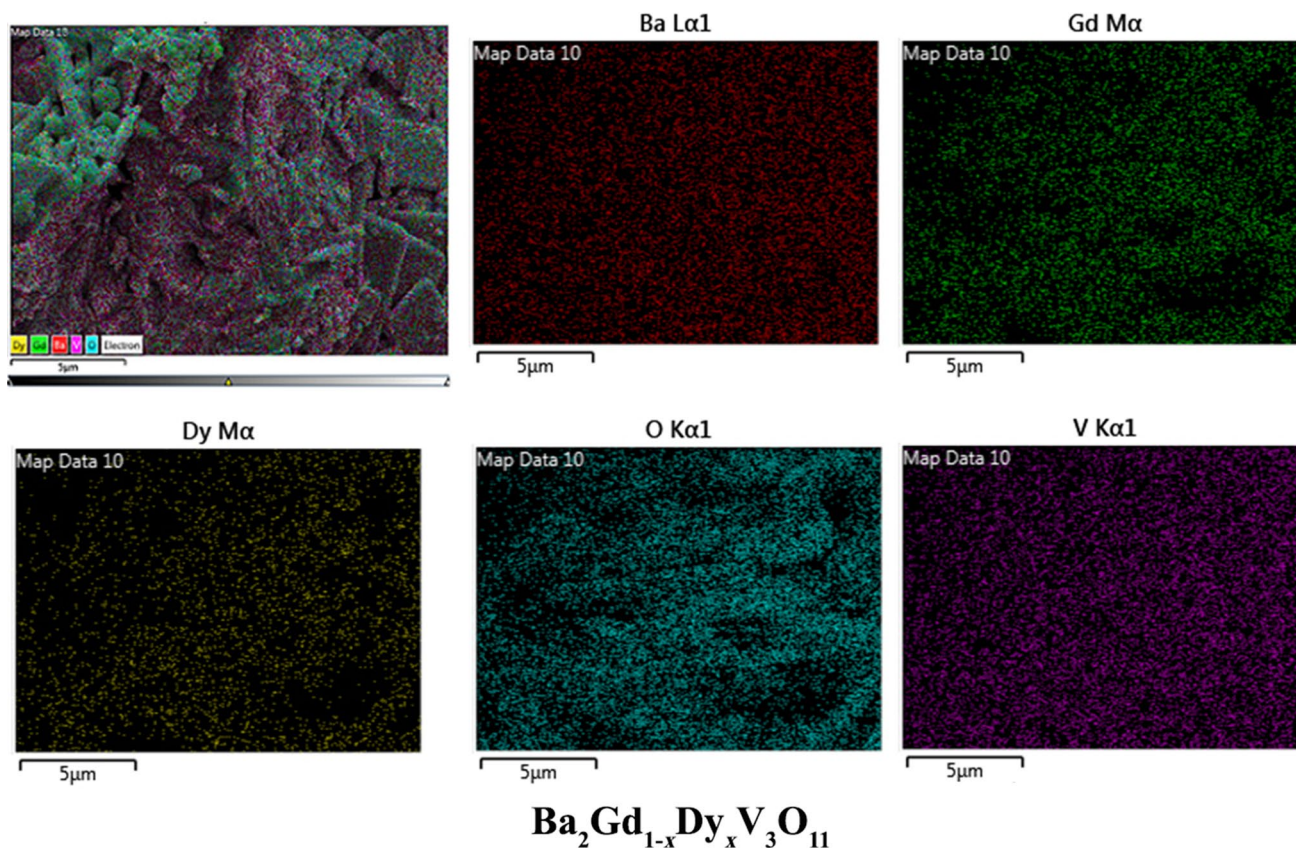
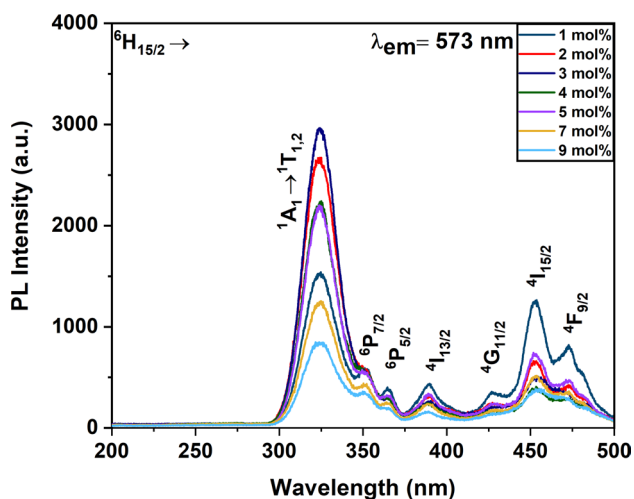


Fig. 6 The elemental mapping of Ba<sub>2</sub>Gd<sub>1-x</sub>Dy<sub>x</sub>V<sub>3</sub>O<sub>11</sub>:Dy<sup>3+</sup> nanophosphor.

for usage in UV-directed WLEDs.<sup>34</sup> The characteristic  $f-f$  transitions attributed to  $\text{Dy}^{3+}$  ions arise from the ground-state  ${}^6\text{H}_{15/2}$  in the excitation spectra (Fig. 7). A report on doped  $\text{Ba}_2\text{GdV}_3\text{O}_{11}$  indicated excitation in the near-infrared region (NIR) with wavelength of 978 nm. Also, the  $\text{Yb}^{3+}$  acts as a sensitizer enhancing absorption of the NIR radiation, whereas the low concentrations of emitters such as  $\text{Er}^{3+}$ ,  $\text{Ho}^{3+}$ , and  $\text{Tm}^{3+}$  with 2, 1, and 0.5 mol% compositions exhibit characteristic  $f-f$  transitions that led to emission in green, orange, and blue regions.<sup>22</sup>



**Fig. 7** Excitation spectra of  $\text{Ba}_2\text{Gd}_{1-x}\text{Dy}_x\text{V}_3\text{O}_{11}$  ( $x = 0.01\text{--}0.09$ ) nanophosphor studied at  $\lambda_{\text{em}} = 573$  nm.

The emission spectra displayed by the  $\text{Dy}^{3+}$ -doped  $\text{Ba}_2\text{GdV}_3\text{O}_{11}$  nanophosphor series on excitation by 324-nm wavelength are represented in Fig. 8 along with the emission curve of  $\text{Ba}_2\text{Gd}_{0.97}\text{Dy}_{0.03}\text{V}_3\text{O}_{11}$  in the inset. The emission spectra encompass two intense peaks as the wavelength proceeds from 400 to 700 nm. A peak at 484 nm arises in the blue zone, whereas the peak centered at 573 nm lies in the yellow zone of the concerned spectra. The former peak is attributed to magnetic dipole type of  ${}^4\text{F}_{9/2} \rightarrow {}^6\text{H}_{15/2}$  transition, and the latter is credited to  ${}^4\text{F}_{9/2} \rightarrow {}^6\text{H}_{13/2}$  which is an electric dipole transition.<sup>35,36</sup> The yellow-to-blue integrated photoluminescence emission intensity ratio for respective compositions of the  $\text{Dy}^{3+}$ -doped  $\text{Ba}_2\text{GdV}_3\text{O}_{11}$  nanophosphor series is listed in Table III. It can be witnessed from the table that the ratio comes out to be closer to unity and bears only small variation. Therefore, different mol% compositions show stability in color display. The emission spectra bear no peak or band because of the  $\text{VO}_4^{3-}$  group of the host. So it indicates that the excitation wavelength of 324 nm after being absorbed by the vanadate group is transferred non-radiatively to the  $\text{Dy}^{3+}$  dopant ions. It aids to the increment in the intensity of the characteristic emission demonstrated by  $\text{Dy}^{3+}$  ions. Also, there occurs a continuous increase in the emission intensity of  $\text{Ba}_2\text{Gd}_{1-x}\text{V}_3\text{O}_{11} : x\text{Dy}^{3+}$  nanophosphor up to  $x = 0.03$  and a decrement afterwards, as displayed in Fig. 10. The concentration quenching phenomenon plays a role in the increment in the emission intensity values up to the optimal fluorescent composition followed by a decline in the same. The various excitation and emission transitions and

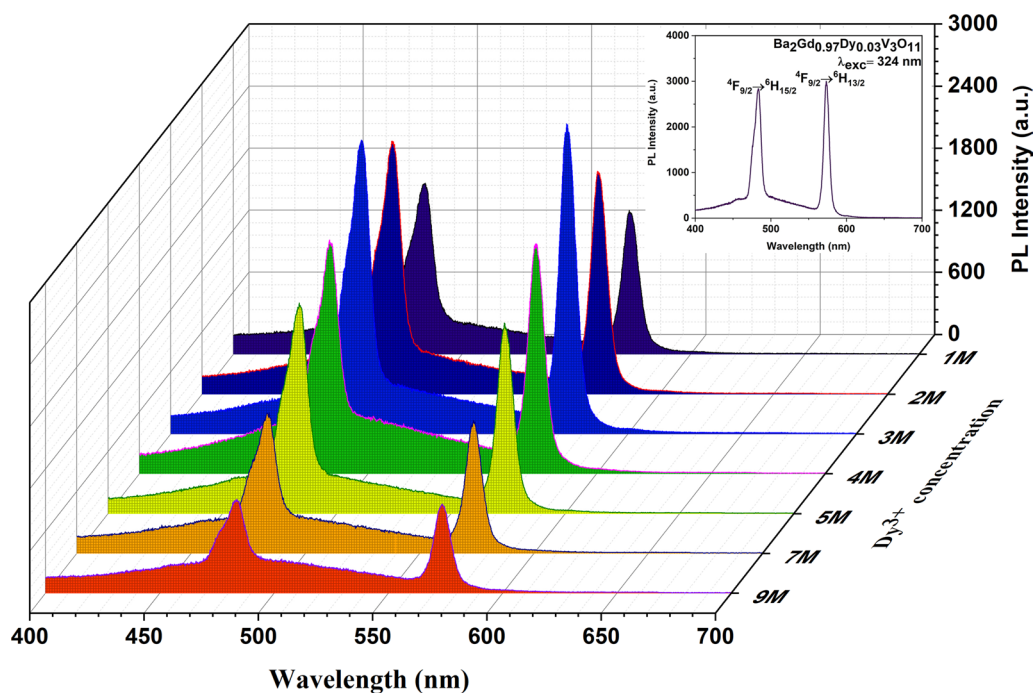


**Fig. 8** Emission spectrum of  $\text{Ba}_2\text{Gd}_{1-x}\text{Dy}_x\text{V}_3\text{O}_{11}$  ( $x = 0.01\text{--}0.09$ ) phosphor at  $\lambda_{\text{ex}} = 324$  nm.



their corresponding wave numbers are listed in Table IV. The Dy<sup>3+</sup>-doped Ba<sub>2</sub>GdV<sub>3</sub>O<sub>11</sub> nanophosphor on excitation at 324 nm exhibited various radiative and non-radiative processes of energy transfer. Figure 9 displays an energy level diagram and is a depiction of all these processes occurring among quantum mechanical term states. The diagram comprises the energy level of the vanadate group of the host and dopant Dy<sup>3+</sup> ion. The VO<sub>4</sub><sup>3-</sup> group consists of <sup>1</sup>A<sub>1</sub> term as ground state, singlets <sup>1</sup>T<sub>1</sub> and <sup>1</sup>T<sub>2</sub> along with triplets <sup>3</sup>T<sub>1</sub> and <sup>3</sup>T<sub>2</sub> as excited states. The nanophosphor, on being supplied with 324 nm of excitation wavelength, exhibited energy absorption by the vanadate group of the host (<sup>1</sup>A<sub>1</sub> → <sup>1</sup>T<sub>1,2</sub> transition) and a successive transfer of this energy to dopant Dy<sup>3+</sup> ions. The emission spectra are deprived of any band credited to the host. Hence, there is no energy transmission among singlet <sup>1</sup>T<sub>1,2</sub> states to triplet <sup>3</sup>T<sub>1,2</sub> states in the VO<sub>4</sub><sup>3-</sup> group. A complete transfer of energy occurs in a non-radiative fashion among <sup>1</sup>T<sub>1,2</sub> states of the vanadate group and term states of dopant Dy<sup>3+</sup> ions. The <sup>6</sup>H<sub>15/2</sub> ground state of trivalent dysprosium ion populates <sup>6</sup>P<sub>7/2</sub>, <sup>6</sup>P<sub>5/2</sub>, <sup>4</sup>I<sub>13/2</sub>, <sup>4</sup>G<sub>11/2</sub>, <sup>4</sup>I<sub>15/2</sub>, and <sup>4</sup>F<sub>9/2</sub> term states on excitation of 351, 365, 389, 427, 453, and 474 nm of wavelength, respectively. These excited term states relax non-radiatively to another excited term state: <sup>4</sup>F<sub>9/2</sub>. Two emission peaks emerge at 484 and 573 nm due to radiative relaxation of the <sup>4</sup>F<sub>9/2</sub> quantum mechanical state to <sup>6</sup>H<sub>15/2</sub> and <sup>6</sup>H<sub>13/2</sub> term states. The intensity of these emission

peaks increases up to 3 mol% composition and decreases afterwards, which is quite similar to that of its Eu<sup>3+</sup>-doped counterpart.<sup>23</sup> In Ba<sub>2</sub>Gd<sub>0.97</sub>Dy<sub>0.03</sub>V<sub>3</sub>O<sub>11</sub> nanophosphor, the critical distance (Å) of energy transfer was calculated by the following equation<sup>37</sup>:

$$R_c = 2 \left[ \frac{3V}{4\pi x_c N} \right]^{1/3} \tag{3}$$

The abovementioned equation comprises R<sub>c</sub> (the critical distance), V (the volume capacity related to the unit cell), x<sub>c</sub> (optimal fluorescent composition), and N (replaceable number of cations per unit cell). In Eq. 3, putting V = 1042.51 Å<sup>3</sup>, x<sub>c</sub> = 0.03, and N = 4, the value of R<sub>c</sub> was obtained as 25.50 Å. For exchange interactions to occur, the condition of R<sub>c</sub> ≤ 5 Å must be met. As far as the obtained value of critical distance, 25.50 Å is considered in the present case; the exchange interactions do not play a role in energy migration.

**Table III** Y/B ratio, CIE 1931 chromaticity coordinates, and CCT of Ba<sub>2</sub>Gd<sub>1-x</sub>Dy<sub>x</sub>V<sub>3</sub>O<sub>11</sub> (x = 0.01–0.09) nanophosphors

Ba <sub>2</sub> Gd <sub>1-x</sub> Dy <sub>x</sub> V <sub>3</sub> O <sub>11</sub> (mol%)	Y/B ratio	CIE coordinates (x,y)	(u', v')	CCT (K)
1	0.59	0.231, 0.304	0.149, 0.442	14,189
2	0.63	0.240, 0.315	0.152, 0.450	12,330
3	0.77	0.256, 0.341	0.155, 0.466	9751
4	0.71	0.240, 0.334	0.147, 0.460	11,195
5	0.65	0.239, 0.321	0.150, 0.453	11,987
7	0.66	0.232, 0.319	0.146, 0.451	12,804
9	0.67	0.226, 0.323	0.141, 0.453	13,016

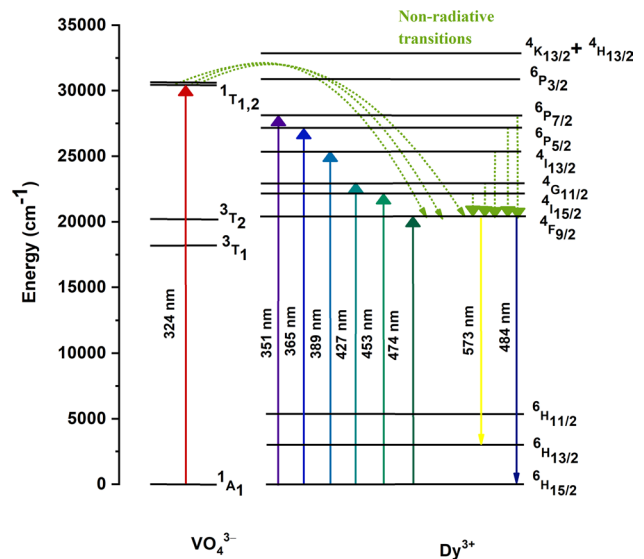


**Fig. 9** Energy level diagram for Dy<sup>3+</sup>-doped Ba<sub>2</sub>GdV<sub>3</sub>O<sub>11</sub> nanophosphor.

**Table IV** Different types of transitions occurring in photoluminescence spectra of Ba<sub>2</sub>Gd<sub>1-x</sub>Dy<sub>x</sub>V<sub>3</sub>O<sub>11</sub> (x = 0.01–0.09) nanophosphors

Nanophosphor	Type of spectrum	Transitions	Wave number (cm <sup>-1</sup> )	Intensity
Ba <sub>2</sub> Gd <sub>0.97</sub> Dy <sub>0.03</sub> V <sub>3</sub> O <sub>11</sub>	Excitation (λ <sub>em</sub> = 573 nm)	<sup>1</sup> A <sub>1</sub> → <sup>1</sup> T <sub>1,2</sub>	30,864.18	Very strong
		<sup>6</sup> H <sub>15/2</sub> → <sup>6</sup> P <sub>7/2</sub>	28,490.02	Medium
		<sup>6</sup> H <sub>15/2</sub> → <sup>6</sup> P <sub>5/2</sub>	27,397.26	Weak
		<sup>6</sup> H <sub>15/2</sub> → <sup>4</sup> I <sub>13/2</sub>	25,706.94	Medium
		<sup>6</sup> H <sub>15/2</sub> → <sup>4</sup> G <sub>11/2</sub>	23,419.20	Weak
		<sup>6</sup> H <sub>15/2</sub> → <sup>4</sup> I <sub>15/2</sub>	22,075.55	Strong
	Emission (λ <sub>ex</sub> = 324 nm)	<sup>6</sup> H <sub>15/2</sub> → <sup>4</sup> F <sub>9/2</sub>	21,097.04	Medium
		<sup>6</sup> F <sub>9/2</sub> → <sup>6</sup> H <sub>15/2</sub>	20,661.16	Strong
		<sup>6</sup> F <sub>9/2</sub> → <sup>6</sup> H <sub>13/2</sub>	17,452.00	Very strong

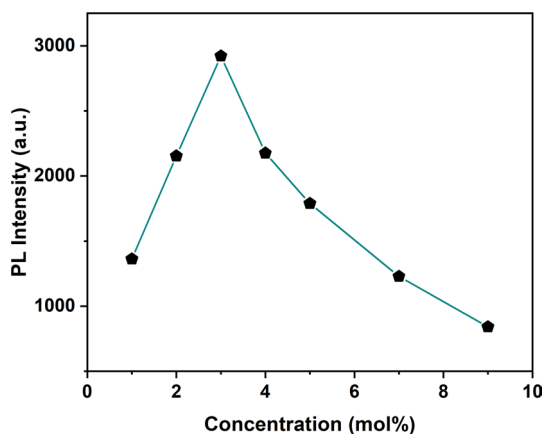


**Fig. 10** Variation of photoluminescence emission intensity as a function of dopant concentration in  $\text{Ba}_2\text{GdV}_3\text{O}_{11}:\text{Dy}^{3+}$  nanophosphor.

Furthermore, the absence of any kind of overlap of bands among excitation and emission spectra rules out the possibility of energy transfer by means of radiative reabsorption. The multipolar interactions led by energy transfer have been indicated by Dexter's theoretical model.<sup>27</sup> The intensity corresponding to the yellow emission at 573 nm displays a decrement post the optimal fluorescent composition of 3 mol% as shown in Fig. 10. This trend is attributed to the phenomenon of concentration quenching and has been explained in the following manner by an equation given by Huang:<sup>38</sup>

$$\log\left(\frac{I}{x}\right) = -\frac{s}{d} \log(x) + \log(f) \quad (4)$$

In Eq. 4, the ratio of the intensity of the emission peak and respective molar concentration of  $\text{Dy}^{3+}$  ions ( $x \geq 0.03$ , the optimal luminescent composition is 3 mol%) is represented by  $I/x$ ; a constant independent of  $x$  is denoted by  $f$ , the dimensions of the sample under study are given by  $d$  ( $= 3$ ), whereas the multipolar interactions in action are represented by a constant  $s$ . The interactions are dependent on a value specific to  $s$ . The constant  $s$  offers a value of six, eight, and ten for dipole–dipole, dipole–quadrupole, and quadrupole–quadrupole interactions to be in action, respectively. Figure 11 conveys a graph between  $\log(I/x)$  and  $\log(x)$  that results into a straight line with a value of  $-2.11$  for the slope. The multipolar interaction constant  $s$  is estimated to bear a value of 6.33 that is closer to the  $s$  value of six for dipole–dipole (d-d) interactions. Therefore, the transfer of energy plus concentration quenching taking place in  $\text{Dy}^{3+}$ -doped  $\text{Ba}_2\text{GdV}_3\text{O}_{11}$  nanophosphor were found to be directed by dipole–dipole interactions rather than from exchange interactions, as witnessed in the reported in literature on  $\text{Eu}^{3+}$ -doped  $\text{Ba}_2\text{GdV}_3\text{O}_{11}$ .<sup>23</sup>

The  $\text{Ba}_2\text{Gd}_{1-x}\text{Dy}_x\text{V}_3\text{O}_{11}$  ( $x = 0.01$ – $0.09$ ) nanophosphor series after excitation undergoes radiative de-excitation

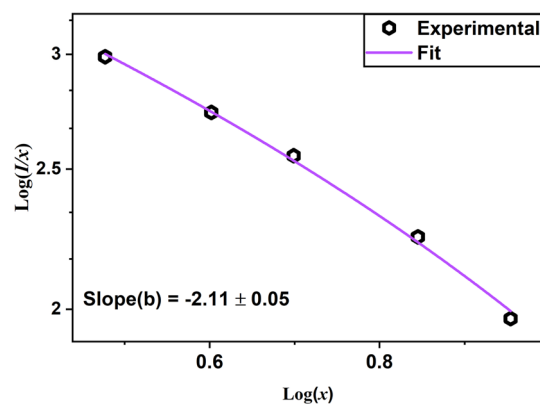


**Fig. 11** Plot of  $\log(I/x)$  as a function of  $\log(x)$  in  $\text{Ba}_2\text{GdV}_3\text{O}_{11}:\text{Dy}^{3+}$  nanophosphor.

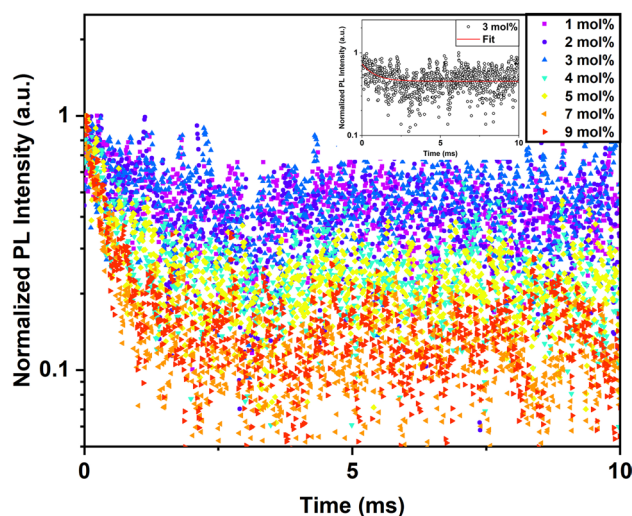


**Fig. 12** The luminescence decay curve for 573-nm ( ${}^4\text{F}_{9/2} \rightarrow {}^6\text{H}_{13/2}$ ) emission of  $\text{Ba}_2\text{Gd}_{1-x}\text{Dy}_x\text{V}_3\text{O}_{11}$  ( $x = 0.01$ – $0.09$ ) nanophosphors.

from its  ${}^4\text{F}_{9/2}$  state. In order to analyze the radiative/relaxation process, the normalized PL intensity associated with the transition, namely,  ${}^4\text{F}_{9/2} \rightarrow {}^6\text{H}_{13/2}$ , at an excitation wavelength of 324 nm was plotted with respect to time (ms). These plots are also known as decay curves. The curves corresponding to the  $\text{Ba}_2\text{Gd}_{1-x}\text{V}_3\text{O}_{11} : x\text{Dy}^{3+}$  ( $x = 0.01$ – $0.09$ ) nanophosphor series are displayed in Fig. 12 along with time-correlated normalized PL intensity of  $\text{Ba}_2\text{Gd}_{0.97}\text{Dy}_{0.03}\text{V}_3\text{O}_{11}$  in the inset. The decay curves displayed by the prepared nanophosphor series fit quite well in the mono-exponential framework of decay function, as given below:

$$I = I_0 \exp(-t/\tau) \quad (5)$$

**Table V** Photoluminescence lifetime, non-radiative rates, and quantum efficiencies of the <sup>4</sup>F<sub>9/2</sub> level in Ba<sub>2</sub>Gd<sub>1-x</sub>Dy<sub>x</sub>V<sub>3</sub>O<sub>11</sub> (x = 0.01–0.09) nanophosphors

Dy <sup>3+</sup> concentration (mol%)	Average lifetime (ms)	Non-radiative rates (s <sup>-1</sup> )	Quantum efficiency (%)
1	0.801 ± 0.131	349.158	72
2	0.763 ± 0.087	409.915	68
3	0.757 ± 0.096	421.178	67
4	0.487 ± 0.026	1153.377	44
5	0.389 ± 0.017	1670.387	35
7	0.367 ± 0.009	1821.685	33
9	0.356 ± 0.010	1907.746	32

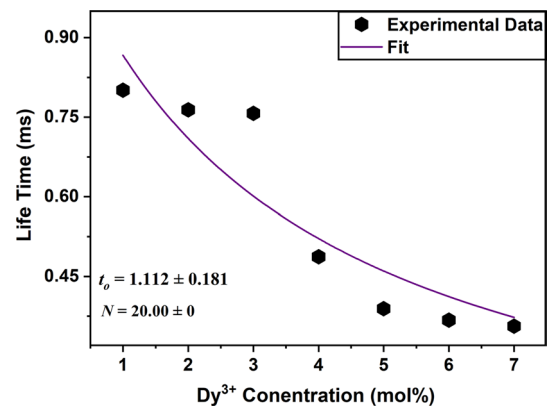
In the aforementioned equation, the mono-exponential function consists of the PL intensity at time  $t$  denoted by  $I$ , the PL intensity at time  $0$  represented by  $I_0$ , and the average lifetime displayed by  $\tau$ . The values for average lifetime related to Ba<sub>2</sub>Gd<sub>1-x</sub>Dy<sub>x</sub>V<sub>3</sub>O<sub>11</sub> (x = 0.01–0.09) nanophosphor series are summarized in Table V, and the values exhibited a decrease from 0.801 ms (1 mol%) to 0.356 ms (9 mol%). This decrement is attributed to non-radiative means of transfer of energy in the synthesized nanophosphor. The different compositions of Ba<sub>2</sub>Gd<sub>1-x</sub>Dy<sub>x</sub>V<sub>3</sub>O<sub>11</sub> (x = 0.01–0.09) nanophosphor indicate the mono-exponential decay conduct (Fig. 12); therefore, Dy<sup>3+</sup> ions inhabit a single type of emission center in Ba<sub>2</sub>GdV<sub>3</sub>O<sub>11</sub> host.

In the trivalent dysprosium-doped Ba<sub>2</sub>GdV<sub>3</sub>O<sub>11</sub> nanophosphor, the values of PL lifetime display a decreasing trend with a raise in concentration from  $x = 0.01$  to  $x = 0.09$ . This conduct was analyzed through Auzel's model via Eq. 6:

$$\tau(c) = \frac{\tau_R}{1 + \frac{c}{c_0} e^{-N/3}} \quad (6)$$

In Eq. 6, the average PL lifetimes correlated to different Dy<sup>3+</sup> proportions are displayed as  $\tau(c)$ ;  $\tau_R$  is the intrinsic lifetime relative to the state that is emitting,  $c_0$  is a constant, whereas  $N$  represents the overall number of phonons that have been generated. The average PL lifetime values were induced and fitted in Eq. 6, and the total number of phonons ( $N = 20.00 \pm 0$ ) drawn out during relaxation of <sup>4</sup>F<sub>9/2</sub> state in a non-radiative way to ground state have been estimated. In Ba<sub>2</sub>GdV<sub>3</sub>O<sub>11</sub> host prototype, the obtained value of  $N$  is analogous to the energy gap in addition to the phonon energy.<sup>23</sup> The greater the number of phonons, the larger will be the rate of radiative decay in the synthesized nanophosphor. Additionally, a lifetime value (1.112 ms) intrinsic to the <sup>4</sup>F<sub>9/2</sub> state was attained (Fig. 13).

The value attained for the intrinsic lifetime was utilized for the estimation of quantum efficiency ( $\phi$ ) for the <sup>4</sup>F<sub>9/2</sub> state analogous to variously doped proportions of


**Fig. 13** Dependence of photoluminescence lifetime of the <sup>4</sup>F<sub>9/2</sub> state on the doping concentration of Dy<sup>3+</sup> through Auzel's model.

Ba<sub>2</sub>Gd<sub>1-x</sub>Dy<sub>x</sub>V<sub>3</sub>O<sub>11</sub> (x = 0.01–0.09) nanophosphor series. The quantum efficiency ( $\phi$ ) can be calculated with the help of intrinsic lifetime value in the following manner<sup>39</sup>:

$$\phi = \frac{\tau}{\tau_R} = \frac{A_R}{A_R + A_{nR}} \quad (7)$$

The intrinsic lifetime value can also be utilized to calculate the rates of relaxation specifically by non-radiative means.<sup>40</sup>

$$\frac{1}{\tau} = \frac{1}{\tau_R} + A_{nR} \quad (8)$$

The above Eqs. 7 and 8 consist of the average lifetime value denoted as  $\tau$  and the intrinsic lifetime value represented as  $\tau_R$ ; the rate of relaxation particularly by non-radiative means is shown as  $A_{nR}$ , and by radiative means is represented by  $A_R$ . In the present case of Ba<sub>2</sub>Gd<sub>1-x</sub>Dy<sub>x</sub>V<sub>3</sub>O<sub>11</sub> (x = 0.01–0.09) nanophosphors, the non-radiative rates (s<sup>-1</sup>) and quantum efficiency values (%) for the emitting state are listed in Table V.

The chromaticity parameters  $x$ ,  $y$  have also been computed so as to analyze the color behavior of the synthesized nanophosphor series of Dy<sup>3+</sup>-doped Ba<sub>2</sub>Gd<sub>1-x</sub>V<sub>3</sub>O<sub>11</sub> (x = 0.01–0.09). The MATLAB software package was used to process the emission spectra of different mol% compositions, and the respective color coordinates ( $x$ ,  $y$ ) have been obtained and listed in Table III. The  $x$  (= 0.256) and  $y$  (= 0.341) coordinates of Ba<sub>2</sub>Gd<sub>0.97</sub>Dy<sub>0.03</sub>V<sub>3</sub>O<sub>11</sub> nanophosphor are conveyed by means of the CIE 1931 chromaticity diagram in Fig. 14 with the UV radiation-triggered color displayed by the optimal fluorescent composition in the inset. The  $x$ ,  $y$  coordinates of other doped proportions are near the value of Ba<sub>2</sub>Gd<sub>0.97</sub>Dy<sub>0.03</sub>V<sub>3</sub>O<sub>11</sub> nanophosphor, and it emits white color that makes it suitable for UV-triggered WLEDs.

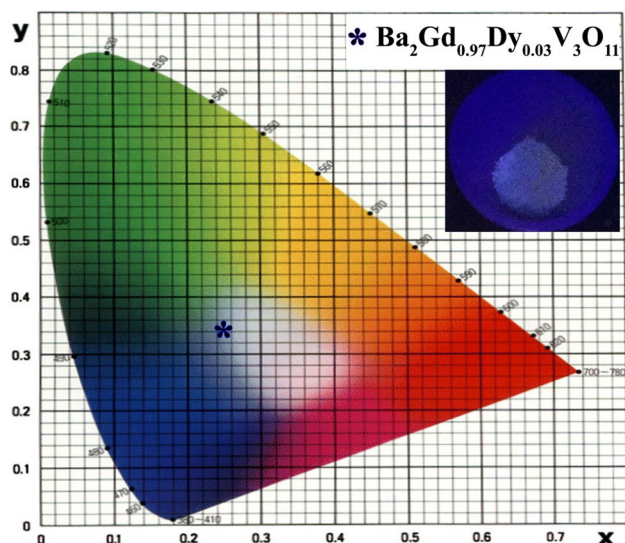


**Fig. 14** CIE chromaticity diagram for  $\text{Ba}_2\text{Gd}_{0.97}\text{Dy}_{0.03}\text{V}_3\text{O}_{11}$  nanophosphor.

Furthermore,  $u'$ ,  $v'$  coordinates and the CCT values were estimated for the optimal luminescent composition of  $0.03\text{Dy}^{3+}:\text{Ba}_2\text{Gd}_{0.97}\text{V}_3\text{O}_{11}$  by means of Eqs. 9, 10 and 11, respectively.<sup>41</sup>

$$u' = \frac{4x}{12y - 2x + 3} \quad (9)$$

$$v' = \frac{9y}{12y - 2x + 3} \quad (10)$$

In abovementioned Eqs. 9 and 10,  $x$  and  $y$  signify the coordinates of  $\text{Ba}_2\text{Gd}_{0.97}\text{Dy}_{0.03}\text{V}_3\text{O}_{11}$  nanophosphor. The values for  $u'$  and  $v'$  come out to be 0.155 and 0.466, respectively.

$$\text{CCT} = -437n^3 + 3601n^2 - 6861n + 5514.31 \quad (11)$$

In Eq. 11, the ratio of  $(x - x_c)$  and  $(y - y_c)$  is represented by  $n$ ;  $x$  and  $y$  are related CIE coordinates for  $\text{Ba}_2\text{Gd}_{0.97}\text{Dy}_{0.03}\text{V}_3\text{O}_{11}$ , whereas  $x_c$  ( $= 0.3320$ ) and  $y_c$  ( $= 0.1858$ ) stand for chromaticity epicenters. The CCT study of  $\text{Ba}_2\text{Gd}_{0.97}\text{Dy}_{0.03}\text{V}_3\text{O}_{11}$  has been conveyed through Fig. 15. The  $u'$ ,  $v'$  and CCT values of more than 5000 K (indicating cool light)<sup>42,43</sup> for the complete nanophosphor series  $\text{Ba}_2\text{Gd}_{1-x}\text{Dy}_x\text{V}_3\text{O}_{11}$  ( $x = 0.01-0.09$ ) are listed in Table III. The CCT was estimated to be 9751 K, turning it into a white light emitter for illumination intent.

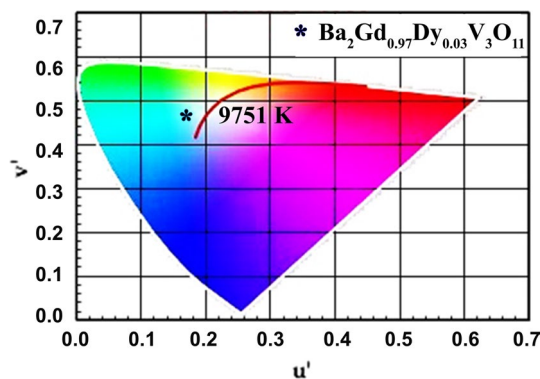


**Fig. 15** CCT study of  $\text{Ba}_2\text{Gd}_{0.97}\text{Dy}_{0.03}\text{V}_3\text{O}_{11}$  nanophosphor.

## Conclusions

Urea-fueled solution combustion was employed to synthesize mono-phased  $\text{Dy}^{3+}$ -doped  $\text{Ba}_2\text{GdV}_3\text{O}_{11}$  nanocrystalline series. The XRD patterns of the synthesized nanophosphors are in accordance to that of standard host. The Rietveld refinement indicates a crystal system (monoclinic) and space group symmetry ( $P21/c$ ). The FE-SEM results ratify the synthesis of rod-shaped nanocrystals, whereas the absence of any impurity was confirmed by EDS analysis. The ultraviolet excitation at 324 nm leads to  ${}^4\text{F}_{9/2} \rightarrow {}^6\text{H}_{13/2, 15/2}$  transitions that are characteristic to dopant  $\text{Dy}^{3+}$  ions. The dipole-dipole (d-d) interactions were found to be accountable for the phenomena of concentration quenching post optimal luminescent composition. The intrinsic lifetime (1.112 ms) and non-radiative rates ( $421.178 \text{ s}^{-1}$ ) were attained by analyzing the mono-exponential conduct of decay curves related to the prepared nanophosphor compositions. The CIE coordinates  $x, y$  (0.256, 0.341) along with correlated color temperature value (9751 K) support the candidature of  $\text{Dy}^{3+}$ -doped  $\text{Ba}_2\text{GdV}_3\text{O}_{11}$  as a white light-emitting component having good quantum efficiency (67%) to be used in lighting devices.

**Acknowledgment** One of the authors, Ms. Priya Phogat, gratefully recognizes the University Grants Commission (UGC), New Delhi, India, for granting support to the research work financially in the form of senior research fellowship (SRF, Award No. 128/ CSIR-UGC NET DEC 2017).

**Conflicts of Interest** The authors of this research article bear no conflicts of interests for declaration.

## References

- N.C. George, K.A. Denault, and R. Seshadri, Phosphors for Solid-State White Lighting. *Annu. Rev. Mater. Res.* 43, 481 (2013).
- A.K. Bedyal, V. Kumar, O.M. Ntwaeaborwa, and H.C. Swart, A promising Orange-Red Emitting Nanocrystalline NaCaBO<sub>3</sub>: Sm<sup>3+</sup> Phosphor for solid State Lightning. *Mater. Res. Express.* 1, 015006 (2014).
- Z. Xu, C. Li, Z. Hou, C. Peng, and J. Lin, Morphological Control and Luminescence Properties of Lanthanide Orthovanadate LnVO<sub>4</sub> (Ln = La to Lu) Nano-/Microcrystals via Hydrothermal Process. *CrystEngComm* 13, 474 (2011).
- Q. Zhao, Y. Zheng, N. Guo, Y. Jia, H. Qiao, W. Lv, and H. You, 3D-Hierarchical Lu<sub>2</sub>O<sub>2</sub>S: Eu<sup>3+</sup> Micro/Nano-Structures: Controlled Synthesis and Luminescence Properties. *CrystEngComm* 14, 6659 (2012).
- F.B. Xiong, C.Y. Han, H.F. Lin, Y.P. Wang, H.Y. Lin, H.X. Shen, and W.Z. Zhu, White Light Emission from Novel Host-Sensitized Single-Phase Y<sub>2</sub>WO<sub>6</sub>: Ln<sup>3+</sup> (Ln<sup>3+</sup>=Eu<sup>3+</sup>, Dy<sup>3+</sup>) Phosphors. *Ceram. Int.* 42, 13841 (2016).
- H. Hafez, M. Saif, and M.S.A. Abdel-Mottaleb, Down-Converting Lanthanide Doped TiO<sub>2</sub> Photoelectrodes for Efficiency Enhancement of Dye-Sensitized Solar Cells. *J. Power Sources.* 196, 5792 (2011).
- K. Li, and R. Van Deun, Photoluminescence and Energy Transfer Properties of a Novel Molybdate KBaY(MoO<sub>4</sub>)<sub>3</sub>: Ln<sup>3+</sup> (Ln<sup>3+</sup> = Tb<sup>3+</sup>, Eu<sup>3+</sup>, Sm<sup>3+</sup>, Tb<sup>3+</sup>/Eu<sup>3+</sup>, Tb<sup>3+</sup>/Sm<sup>3+</sup>) as a Multi-Color Emitting Phosphor for UV w-LEDs. *Dalton Trans.* 47, 6995 (2018).
- S. Dutta, S. Som, and S.K. Sharma, Luminescence and Photometric Characterization of K<sup>+</sup> Compensated CaMoO<sub>4</sub>: Dy<sup>3+</sup> Nanophosphors. *Dalton Trans.* 42, 9654 (2013).
- G. Sharma, D.H. Sang, S.P. Khatkar, V.B. Taxak, W.R. Young, Luminescent Properties of ZnS: Eu<sup>2+</sup> Nanocrystals, *ECS Trans.* 1, 7 (2006)
- Y. Lin, Z. Tang, Z. Zhang, and C.W. Nan, Anomalous Luminescence in Sr<sub>4</sub>Al<sub>14</sub>O<sub>25</sub>: Eu, Dy Phosphors. *Appl. Phys. Lett.* 81, 996 (2002).
- P. Phogat, S.P. Khatkar, V.B. Taxak, and R.K. Malik, Sm<sup>3+</sup> Doped Bi<sub>4</sub>MgO<sub>4</sub>(PO<sub>4</sub>)<sub>2</sub>: Crystal and Optoelectronic Investigation of the Solution Combustion Derived Bright Orange Emanating Novel Nanophosphor for SSLs. *Mater. Chem. Phys.* 276, 125389 (2022).
- Z. Xia, J. Zhou, and Z. Mao, Near UV-Pumped Green-Emitting Na<sub>3</sub>(Y, Sc)Si<sub>3</sub>O<sub>9</sub>: Eu<sup>2+</sup> Phosphor for White-Emitting Diodes. *J. Mater. Chem. C.* 1, 5917 (2013).
- K. Tadatomo, M. Kato, H. Okagawa, M. Harada, T. Jyoichi, and T. Taguchi, Development of White LED Fabricated by RGB Phosphor and Near Ultra-Violet LED. *Mitsubishi Cable Ind. Rev.* 99, 35 (2002).
- J. Liang, L. Sun, G. Annadurai, B. Devakumar, S. Wang, Q. Sun, J. Qiao, H. Guo, B. Li, and X. Huang, Synthesis and Photoluminescence Characteristics of High Color Purity Ba<sub>3</sub>Y<sub>4</sub>O<sub>9</sub>: Eu<sup>3+</sup> Red-Emitting Phosphors with Excellent Thermal Stability for Warm W-LED Application. *RSC Adv.* 8, 32111 (2018).
- Y. Guan, Y. Huang, T. Tsuboi, W. Huang, C. Chen, P. Cai, and H.J. Seo, Conversion and Quantum Efficiency from Ultraviolet Light to Near Infrared Emission in Yb<sup>3+</sup>-Doped Pyrovanadates MZnV<sub>2</sub>O<sub>7</sub> (M = Ca, Sr, Ba). *Mater. Sci. Eng. B.* 190, 26 (2014).
- P. Phogat, S.P. Khatkar, V.B. Taxak, and R.K. Malik, Eu<sup>3+</sup> Incorporated Bi<sub>4</sub>MgO<sub>4</sub>(PO<sub>4</sub>)<sub>2</sub>: Derivation of the Novel Nanophosphor by Solution Combustion and Investigation in to Crystallographic and Photometric Characteristics. *Solid State Sci.* 124, 106799 (2022).
- S. Wang, B. Devakumar, Q. Sun, J. Liang, and L. Sun, Highly Efficient Near-UV-Excitable Ca<sub>2</sub>YHf<sub>2</sub>Al<sub>3</sub>O<sub>12</sub>: Ce<sup>3+</sup>, T<sup>b3+</sup>+ Green-Emitting Garnet Phosphors with Potential Application in High Color Rendering Warm-White LEDs. *J. Mater. Chem. C.* 8, 4408 (2020).
- P. Phogat, S.P. Khatkar, R.K. Malik, J. Dalal, M. Punia, and V.B. Taxak, Crystal Structure and Photoluminescent Analysis of Bright Orange-Red Emanating Sm-Doped Ca<sub>9</sub>Bi(VO<sub>4</sub>)<sub>7</sub> Nanophosphor for WLEDs. *J. Mater. Sci. Mater. Electron.* 32, 1 (2021).
- Q. Su, Z. Pei, Q. Zeng, L. Chi, S.Z. Liu, J. Lin, S.P. Wang, and Y. Lu, Phosphors Doped with Dy<sup>3+</sup> and Gd<sup>3+</sup> for Lighting. *Mater. Sci. Forum.* 315–317, 228 (1999).
- M. Dalal, J. Dalal, S. Chahar, H. Dahiya, S. Devi, P. Dhankhar, S. Kumar, V.B. Taxak, D. Kumar, and S.P. Khatkar, A Hybrid Treatment of Ba<sub>2</sub>LaV<sub>3</sub>O<sub>11</sub>: Eu<sup>3+</sup> Nanophosphor System: First-Principal and Experimental Investigations Into Electronic, Crystal and the Optical Structure. *J. Alloys Compd.* 805, 84 (2019).
- Y. Lin, Z. Tang, Z. Zhang, C.W. Nan, Anomalous Luminescence in Sr<sub>4</sub>Al<sub>14</sub>O<sub>25</sub>: Eu, Dy Phosphors. *Appl. Phys. Lett.* 81, 996 (2002)
- N. Kaczorowska, A. Szczeszak, and S. Lis, Synthesis and Tunable Emission Studies of New Up-Converting Ba<sub>2</sub>GdV<sub>3</sub>O<sub>11</sub> Nanopowders Doped with Yb<sup>3+</sup>/Ln<sup>3+</sup> (Ln<sup>3+</sup> = Er<sup>3+</sup>, Ho<sup>3+</sup>, Tm<sup>3+</sup>). *J. Lumin.* 200, 59 (2018).
- J. Dalal, M. Dalal, S. Devi, P. Dhankhar, A. Hooda, A. Khatkar, V.B. Taxak, and S.P. Khatkar, Structural and Judd-Ofelt Intensity Parameters of a Down-Converting Ba<sub>2</sub>GdV<sub>3</sub>O<sub>11</sub>:Eu<sup>3+</sup> Nanophosphors. *Mater. Chem. Phys.* 243, 122631 (2020).
- S. Ekambaram, K.C. Patil, and M. Maaza, Synthesis of Lamp Phosphors: Facile Combustion Approach. *J. Alloys Compd.* 393, 81 (2005).
- M. Dalal, S. Chahar, J. Dalal, R. Devi, D. Kumar, S. Devi, V.B. Taxak, A. Khatkar, M. Kumar, and S.P. Khatkar, Energy Transfer and Photoluminescent Analysis of a Novel Color-Tunable Ba<sub>2</sub>Y<sub>1-x</sub>V<sub>3</sub>O<sub>11</sub>: xSm<sup>3+</sup> Nanophosphor for Single-Phased Phosphor-Converted White LEDs. *Ceram. Int.* 44, 10531 (2018).
- K. Li, H. Lian, M. Shang, and J. Lin, A Novel Greenish Yellow-Orange Red Ba<sub>3</sub>Y<sub>4</sub>O<sub>9</sub>: Bi<sup>3+</sup>, Eu<sup>3+</sup> Phosphor with Efficient Energy Transfer for UV-LEDs. *Dalton Trans.* 44, 20542 (2015).
- S. Chahar, R. Devi, M. Dalal, P. Boora, V.B. Taxak, and S.P. Khatkar, Structural and Photoluminescent Analysis in Judd-Ofelt Framework of Color Tunable SrGd<sub>2(1-x)</sub>Eu<sub>2x</sub>Al<sub>2</sub>O<sub>7</sub> Nanophosphor for White Light Emitting Materials. *J. Lumin.* 194, 271 (2018).
- M. Jaboyedoff, B. Kübler, and P. Thelin, An Empirical Scherrer Equation for Weakly Swelling Mixed-Layer Minerals, Especially Illite-Smectite. *Clay Miner.* 34, 601–617 (1999). <https://doi.org/10.1180/000985599546479>.
- C. Pratap Kumar, S.C. Prashantha, H. Nagabhushana, M.R. Anilkumar, C.R. Ravikumar, H.P. Nagaswarupa, and D.M. Jnaneshwara, White Light Emitting Magnesium Aluminate Nanophosphor: Near Ultra Violet Excited Photoluminescence, Photometric Characteristics and Its UV Photocatalytic Activity. *J. Alloys Compd.* 728, 1124 (2017).
- S.J. Park, J.Y. Kim, J.H. Yim, N.Y. Kim, C.H. Lee, S.J. Yang, and H.K. Yang, The effective Fingerprint Detection Application using Gd<sub>2</sub>Ti<sub>2</sub>O<sub>7</sub>: Eu<sup>3+</sup> Nanophosphors. *J. Alloys Compd.* 741, 246 (2018).
- J. Dalal, A. Khatkar, M. Dalal, S. Chahar, P. Phogat, V.B. Taxak, and S.P. Khatkar, Ba<sub>2</sub>YV<sub>3</sub>O<sub>11</sub>: Eu<sup>3+</sup>—Density Functional and Experimental Analysis of Crystal, Electronic and Optical Properties. *J. Alloys Compd.* 821, 153471 (2020).
- X. Huang and H. Guo, A novel Highly Efficient Single-Composition Tunable White-Light-Emitting LiCa<sub>3</sub>MgV<sub>3</sub>O<sub>12</sub>: Eu<sup>3+</sup> Phosphor. *Dyes Pigm.* 154, 82 (2018).
- P. Phogat, S.P. Khatkar, R.K. Malik, S. Devi, J. Dalal, P. Hooda, V.B. Taxak, Crystal Chemistry and Photoluminescent Investigation of Novel White Light Emanating Dy<sup>3+</sup> Doped Ca<sub>9</sub>Bi(VO<sub>4</sub>)<sub>7</sub> Nanophosphor for Ultraviolet Based White LEDs. *Mater. Chem. Phys.* 124828 (2021).

34. D.K. Singh and J. Manam, Investigation of Structural, Spectral and Photometric Properties of  $\text{CaTiO}_3$ :  $\text{Dy}^{3+}$  Nanophosphors for the Lighting Applications. *Electron. Mater. Lett.* 13, 292 (2017).
35. A. Kumar, S.J. Dhoble, D.R. Peshwe, J. Bhatt, J.J. Terblans, and H.C. Swart, Crystal Structure, Energy Transfer Mechanism and Tunable Luminescence in  $\text{Ce}^{3+}/\text{Dy}^{3+}$  Coactivated  $\text{Ca}_{20}\text{Mg}_3\text{Al}_{26}\text{Si}_3\text{O}_{68}$  Nanophosphors. *Ceram. Int.* 42, 10854 (2016).
36. Y. Tian, B. Chen, B. Tian, R. Hua, J. Sun, L. Cheng, H. Zhong, X. Li, J. Zhang, Y. Zheng, T. Yu, L. Huang, and Q. Meng, Concentration-Dependent Luminescence and Energy Transfer of Flower-Like  $\text{Y}_2(\text{MoO}_4)_3$ : $\text{Dy}^{3+}$  Phosphor. *J. Alloys Compd.* 509, 6096 (2011).
37. P. Phogat, S.P. Khatkar, R.K. Malik, J. Dalal, A. Hooda, and V.B. Taxak, Crystallographic and Judd-Ofelt Parametric Investigation into  $\text{Ca}_9\text{Bi}(\text{VO}_4)_7$ : $\text{Eu}^{3+}$  Nanophosphor for NUV-WLEDs. *J. Lumin.* 234, 117984 (2021).
38. X. Huang, Preparation and Luminescence Characteristics of Monazite  $\text{Eu}^{3+}$ :  $\text{LaPO}_4$  Nanocrystals in  $\text{NH}_4\text{NO}_3$  Molten Salt. *Opt. Mater.* 50, 81 (2015).
39. C.A. Kodaira, H.F. Brito, and M.C.F.C. Felinto, Luminescence Investigation of  $\text{Eu}^{3+}$  ion in the  $\text{RE}_2(\text{WO}_4)_3$  Matrix (RE = La and Gd) Produced Using the Pechini Method. *J. Solid State Chem.* 171, 401 (2003).
40. M.H.V. Werts, R.T.F. Jukes, and J.W. Verhoeven, The Emission Spectrum and the Radiative Lifetime of  $\text{Eu}^{3+}$  in Luminescent Lanthanide Complexes. *Phys. Chem. Chem. Phys.* 4, 1542 (2002).
41. G.P. Darshan, H.B. Premkumar, H. Nagabhushana, S.C. Sharma, S.C. Prashantha, H.P. Nagaswarup, and B.D. Prasad, Blue Light Emitting Ceramic Nano-Pigments of  $\text{Tm}^{3+}$  Doped  $\text{YAlO}_3$ : Applications in Latent Finger Print, Anti-Counterfeiting and Porcelain Stoneware. *Dyes Pigm.* 131, 268 (2016).
42. R. Shrivastava, J. Kaur, and M. Dash, Studies on White Light Emission of  $\text{Sr}_2\text{MgSi}_2\text{O}_7$  Doped with  $\text{Dy}^{3+}$  Phosphors. *Superlattices Microstruct.* 82, 262 (2015).
43. M. Bharathy, V.A. Rassolov, and H.C. Loye, Crystal Growth of  $\text{Sr}_3\text{NaNbO}_6$  and  $\text{Sr}_3\text{NaTaO}_6$ : New Photoluminescent Oxides. *Chem. Mater.* 20, 2268 (2008).

**Publisher's Note** Springer Nature remains neutral with regard to jurisdictional claims in published maps and institutional affiliations.